NANO · MICRO small
www.small-journal.com

Materials and Interface Designs of Waterproof Field-Effect Transistor Arrays for Detection of Neurological Biomarkers

*Yan Dong, Shulin Chen, Tzu-Li Liu, and Jinghua Li**

The continuous, real-time, and concurrent detection of multiple biomarkers in bodily fluids is of high significance for advanced healthcare. While active, semiconductor-based biochemical sensing platforms provide levels of functionality exceeding those of their conventional passive counterparts, the stability of the active biosensors in the liquid environment for continuous operation remains a challenging topic. This work reports the development of a class of flexible and waterproof field-effect transistor arrays for multiplexed biochemical sensing. In this design, monolithic, ultrathin, dense, and low defect nanomembranes consisting of monocrystalline Si and thermally grown SiO_2 simultaneously serve as high-performance backplane electronics for signal transduction and stable biofluid barriers with high structural integrity due to the high formation temperature. Coupling the waterproof transistors with various ion-selective membranes through the gate electrode allows for sensitive and selective detection of multiple ions as biomarkers for traumatic brain injury. The study also demonstrates a similar encapsulation structure which enables the design of waterproof amperometric sensors based on this materials strategy and integration scheme. Overall, key advantages in flexibility, stability, and multifunctionality highlight the potential of using such electronic sensing platforms for concurrent, continuous detection of various neurological biomarkers, proving a promising approach for early diagnosis and intervention of chronic diseases.

1. Introduction

Hundreds of biomarkers exist in bodily fluids which provide abundant information for disease diagnosis and treatment. Of particular interest is biosensing in neuroscience and neuroengineering where the sensitive and selective detection of multiple biological markers is important for real-time, continuous monitoring of metabolic homeostasis as well as the diagnosis of impairments or deviations from normal health status.[1] For example, the secondary damage from traumatic brain injury (TBI) develops through spreading depolarizations (SD) which cause an increasing K^+ concentration and a decreasing Na^+ concentration in cerebrospinal fluid (CSF).[2,3] Therefore, the selective, precise, and concurrent detection of multiple ions in CSF and extracellular fluid (ECF) is essential for the monitoring of disruption of cortical functions, and thus could help save ischemic but potentially viable cerebral tissues.[1] In another example, dopamine (DA) is a type of neurotransmitter which plays an important role in reward, motivation, memory, attention, and movement regulation in the brain. These examples, out of many, highlight the need for developing bio-integrated sensing platforms and technologies with high reliability and stability that can track biomarker levels continuously in liquid environment.[4–6] The capture, analysis, and "mining" of such health data are crucial to tracking long-lasting health conditions for early intervention and treatment of diseases.

Among all types of chemical sensors, active, semiconductor-based ones have attracted considerable attention with levels of functionality exceeding those of conventional passive counterparts.[7,8] Taking ion sensing as an example, compared to conventional ion-selective electrodes (ISEs),[9] ion-selective field-effect transistors (ISFETs) allow for local signal pre-amplification, processing, and multiplexing,[1,10] and thus serve as promising candidates of building components for advanced neural interfaces.[11,12] Previous studies demonstrate the use of a variety of low dimensional thin-film semiconductors (e.g., carbon nanotubes, graphene, MoS_2, black phosphorus) and device structures for chemical and biological sensing.[13–15] For example, Zhang et al. reported wafer-scale, high-performance carbon nanotube transistors for label-free detection of multiple disease biomarkers.[16] Zhou et al. reported flexible In_2O_3 transistor arrays functionalized with enzymes or aptamers for detecting glucose or neurotransmitters.[17–19] The great success of the pioneering works sets the foundation for the application of active biosensors in label-free, ultrasensitive detection of biomarkers in healthcare and biomedical research.

Y. Dong, S. Chen, T.-L. Liu
Department of Materials Science and Engineering
The Ohio State University
Columbus, OH 43210, USA
J. Li
Department of Materials Science and Engineering
Chronic Brain Injury Program
The Ohio State University
Columbus, OH 43210, USA
E-mail: li.11017@osu.edu

The ORCID identification number(s) for the author(s) of this article can be found under https://doi.org/10.1002/smll.202106866.

DOI: 10.1002/smll.202106866

However, the following issues are worth further investigation for in vivo application of field-effect transistor (FET)-based chemical sensors in neuroscience and other healthcare-related fields: 1) The operation of FET chemical sensors involves continuously applied voltages and induced currents immediately adjacent to biofluids. The development of reliable, corrosion-resistive, and bio-integrated potentiometric and amperometric sensors for detecting various biomarkers (e.g., ions, neurotransmitters, and metabolites) is a challenging topic.[20,21] 2) Aside from the stability of electronics, another bottleneck for continuous biochemical sensing is in the sensor-biology interfaces, as the limited stability of bio-recognition elements in biofluids might result in the loss of sensor function well before the electronic devices fail. In the context of ion sensing, the longevity, failure mechanism, and structure-property interrelationship of ion-selective membranes (ISMs) under physiological conditions remain understudied. 3) Achieving concurrent detection of multiple biomarkers with high accuracy in mixed solution also requires further attention, as the crosstalk between sensors can frustrate quantitative interpretation of recorded data.

To solve these problems, this study reports the design of a class of multiplexed biochemical sensor arrays compatible with potentiometric and amperometric sensing based on pioneering studies.[22] Here, ultrathin, yet dense, and low-defect nanomembranes derived from monocrystalline Si serve as waterproof encapsulation protecting the transistors against corrosion when placed in a liquid environment. For potentiometric sensors, gate electrodes functionalized with various ISMs work as interfaces for selective ion capture. By using ISMs for H^+, Na^+, K^+, and Ca^{2+} as examples, the study establishes the proof-of-concept and develops calibration standards based on the cross-sensitivity between different ions and ISMs. In addition to potentiometric sensors, the study further demonstrates that an encapsulation structure consisting of a heavily doped Si nanomembrane can serve as a conductive pathway for electrical currents produced by electrochemical reactions (e.g., DA/serotonin oxidation), thereby enabling the design of amperometric sensors based on this materials strategy and integration scheme.

The system presents an unprecedented combination of the following features: 1) on-chip FETs that could support local signal processing/amplification; 2) waterproof encapsulation derived from monocrystalline Si for sustained operation in liquid environment. The encapsulation consists of insulating SiO_2 and heavily doped, highly conductive Si, which allows for potentiometric and amperometric sensing towards different types of analytes via proper design and integration; 3) versatile, modularized chemical sensor arrays with calibration standards for minimizing crosstalk; 4) high mechanical compliance and minimal invasiveness needed to successfully interrogate soft, dynamic tissues and organs. Integration of such flexible, waterproof, and multifunctional biochemical sensors can form high-resolution neural interfaces which may shift the current paradigm of biochemical sensing from few points describing acute medical concerns to actively multiplexed operating to address processes over extended periods. Compared to other biochemical sensors with active components, one unique advantage is that the current device scheme/fabrication exploits SiO_2 derived from monocrystalline Si as encapsulation with a very high structural integrity. An integrated system following the design scheme could provide better stability for in vivo applications. Additionally, the calibration standards reported here can address the crosstalk issue for biochemical sensing in a complex environment.

2. Results and Discussion

2.1. Design Principles of Flexible, Waterproof, and "Modularized" Transistor Arrays

The design concept of the multifunctional, "modularized", and waterproof transistor arrays and an envisioned application appear in **Figure 1**. Briefly, devices of this type consist of two key functional parts: biochemical interfaces (i.e., ISMs) for capturing target analytes (i.e., ions) (Figure 1A) and Si FET backplanes with monocrystalline Si derived nanomembranes as a waterproof encapsulation (Figure 1B). The ionophores in ISMs can be predominantly complex with a specific ionic species in solution. For example, the K^+ ionophore, valinomycin, is a cyclodepsipeptide composed of twelve alternating amino acids and esters (Figure S1, Supporting Information). The intramolecular hydrogen bonds between the carbonyl O atoms and N—H in the neighboring amide groups result in a rigid ring structure with a cavity in the center for the capture of K^+.[23,24] The interactions between Na^+ and Ca^{2+} ionophores and the corresponding target ions follow a similar mechanism, while H^+ ionophore has a high affinity to H^+ due to the basicity of amine (Figure S1, Supporting Information).[25] The concentration gradient results in a diffusion layer and accordingly a potential difference ψ between the membrane and the bulk electrolyte according to the Nernst equation.[9,26]

Figure 1B shows the cross-section schematic illustration of a Si-FET with a biofluid barrier prepared by a unique "inverted fabrication" method (details in Experimental Section and Figure S2, Supporting Information): briefly, fabricating transistors using device-grade Si nanomembranes (thickness: ≈100–200 nm) on a silicon-on-insulator (SOI) substrate and removing the back-layer Si handle wafer using reactive ion etching (RIE) yield a flexible system with a layer of thermally grown, buried SiO_2 (BOX layer, t-SiO_2, thickness: ≈300–1000 nm) protecting the transistor from biofluids. Etching a window on the BOX layer exposes a pre-patterned island of heavily doped, highly conductive Si (p-type, boron-doped, concentration: ≈10^{20} cm^{-3}, sheet resistance: ≈50–80 ohm sq^{-1}) with metal interconnects formed during the transistor fabrication steps to the gate dielectrics of the encapsulated transistors. Such a monocrystalline Si layer serves as a conductive pathway bridging the electronics side and the biofluid side. Please note that for potentiometric sensors working based on surface potential modulation, opening the window on t-SiO_2 to expose the highly conductive Si interconnect is not a required step. However, establishing such a conductive pathway can minimize the voltage division effect caused by the insulating t-SiO_2 encapsulation layer for obtaining a maximal sensitivity. A polyimide film serves as the flexible substrate for the transistor. The total thickness of the sensor is ≈20 μm. As illustrated in Figure 1A (right),

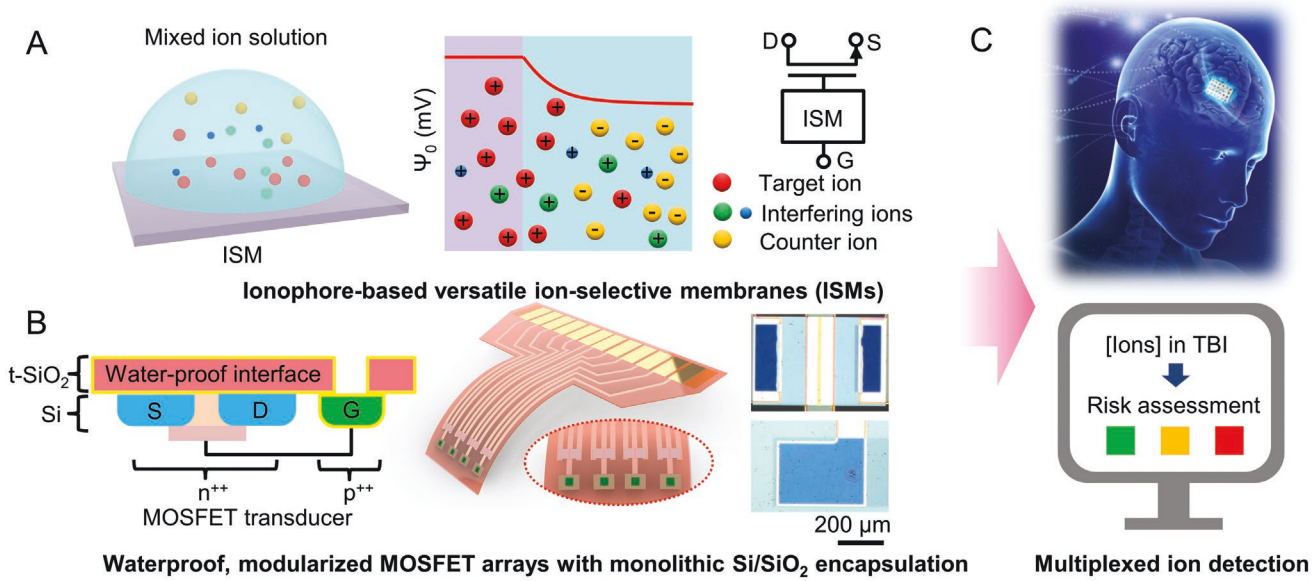

Figure 1. A) Schematic illustration of ISMs as biochemical interfaces and the working principle for ion capture and detection. B) Schematic illustration and optical images of flexible potentiometric sensor arrays with the waterproof encapsulation derived from monocrystalline Si nanomembranes. C) Envisioned application of the device concept in real-time monitoring of TBI biomarkers for early warning, risk assessment, and prediction of patient outcomes.

coupling receptors to the gate electrode can shift the threshold voltage of the transistor (V_{th}) upon the binding of analytes (Note S1, Supporting Information). In this study, we separately prepare the transistor part and the ISM-functionalized gate electrode part and link them together for systematic bench tests so that FETs can be recycled after each use.[27,28] Iterative eliminations suggest that the interface structure of the functionalized gate plays a key role in the sensing performance: sensing layers exploiting the combination of ISMs and Au on the bottom provide the most stable sensing outcomes due to the inertness of Au which minimizes nonspecific interactions. On the other hand, direct coating of ISMs on heavily doped Si does not yield a stable interface for potentiometric sensing which might be due to the active hydroxyl groups on the native oxide that can cause non-specific interactions. Figure 1C shows a potential application of multifunctional sensor arrays based on this device concept, which can interrogate brain tissues and continuously detect changes in ion concentrations in CSF emerging at the secondary stage of TBI as early warning signals of the condition worsening.

2.2. Results of Leakage Tests and Bending Tests

The monocrystalline Si-derived thin-film encapsulation with high structural integrity due to the high formation temperature (> 1000 °C) can significantly improve the stability of encapsulated electronics in a liquid environment.[22,29,30] **Figure 2**A presents a scanning electron microscopy (SEM) image of the top surface of t-SiO_2 after the back etching process. Measuring the time evolution of leakage current across a t-SiO_2 film in solution under elevated temperatures evaluates the stability of the barrier material. All samples used have an area at the same order of magnitude (≈1 cm^2) with only minor variations. Normalizing the leakage current according to the test area further minimizes discrepancies. The initial current is ≈10^{-11} A cm^{-2} and remains constant before a catastrophic failure takes place. A sudden increase in the current corresponds to a leakage event caused by the penetration of biofluids (Figure 2B): a ≈300 nm t-SiO_2 show an average lifetime of ≈1, 2, 4, 10, and 21 days at 95, 91, 87, 81 and 77 °C, respectively. The reason for choosing the elevated temperatures is to allow for assessments of reaction rates that are too low at body or room temperature within a reasonable period (e.g., one month). Calibrating the actual temperatures of the oven during the leakage tests yields the values used for plotting. The results are in qualitative agreement with previous studies while minor differences are associated with the temperature control and the volume of solutions used.[22,31] Linearly fitting the reaction rate as a function of T^{-1} in a semilogarithmic scale extrapolates the reaction rates at lower temperatures according to the Arrhenius equation (Figure 2C)[22] (Note S2, Supporting Information). Calculated lifetimes based on extrapolated reaction rate at different temperatures for a 100, 170, 240, 500, and 1000 nm t-SiO_2 encapsulation appear in Figure 2D. The theory behind using the reaction rate to predict the lifetime t-SiO_2 with different thicknesses is based on previous studies that the failure of t-SiO_2 in liquid is mainly due to the spatially uniform dissolution with an almost constant dissolution rate throughout the process.[22] We also study the pH effects on the dissolution of t-SiO_2. As shown in Figure 2B, under pH 7.4, leakage happens after 2 days, while under alkaline condition (pH = 10.0), leakage happens after only 1 day (Figure S3A, Supporting Information). In acidic PBS solution (pH = 4.0), no leakage event takes place within 7 days as a higher concentration of protons will shift the chemical equilibrium of the reaction producing silicic acids.[32]

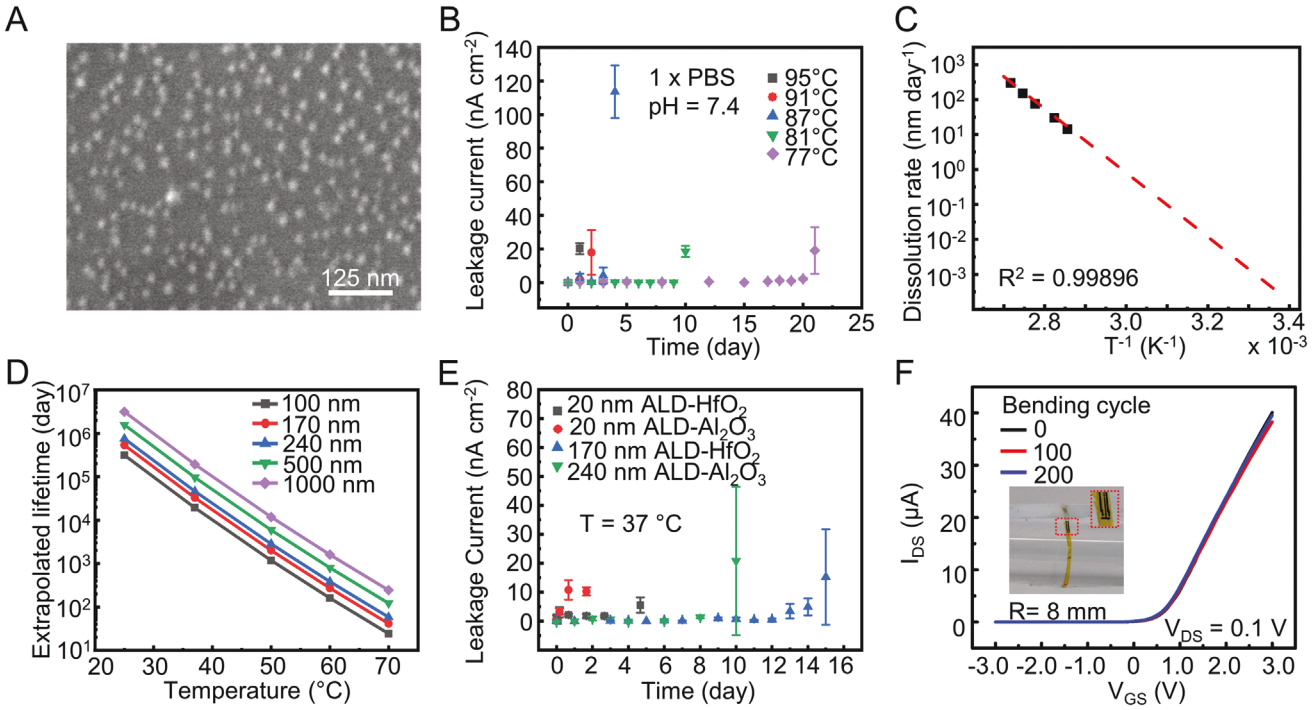

Figure 2. A) SEM image of t-SiO_2 surface after the back etching process with RIE. B) Leakage test results for systems encapsulated with t-SiO_2 nanomembranes (thickness: ≈300 nm) at 95, 91, 87, 81, and 77 °C, respectively (n = 3). C) Experimental and simulated results of reaction rate of t-SiO_2 in PBS solution as a function of T^{-1} according to the Arrhenius' equation. D) Lifetime based on extrapolated reaction rate at different temperatures for a 100, 170, 240, 500, and 1000 nm t-SiO_2 encapsulation. E) Leakage test results for systems encapsulated with 20 and 240 nm ALD-Al_2O_3, 20 and 170 nm HfO_2 at 37 °C (n = 3). F) Bending test results for a transistor encapsulated with ≈1 μm t-SiO_2. Inset: photograph of a test transistor laminated on a glass tube (bending radius = 8 mm). Data presentation: mean ± standard deviation.

In addition to hydrolysis, SiO_2 is also stable against decomposition as determined by its Gibbs free energy of formation (Note S3 and Table S1, Supporting Information) and oxidation as it is in the highest oxidation state. The results suggest that a submicron encapsulation can provide sufficient longevity (at least a few years) to support the operation of active electronics well beyond the lifetime of bio-recognition elements. In comparison, encapsulations of 20 nm Al_2O_3 and HfO_2 prepared by atomic layer deposition (ALD) show a lifetime of only <4 day at 37 °C before leakage events appear (defined as >1 nA cm^{-2}) (Figure 2E). Thicker Al_2O_3 (240 nm) and HfO_2 (170 nm) prepared by ALD have longer lifetimes (10 days for 240 nm ALD Al_2O_3 and 14 days for 170 nm ALD HfO_2). However, these values are still significantly shorter than the predicted lifetimes of 240 nm and 170 nm t-SiO_2 at 37 °C (Figure 2D, 46 250 and 32 760 days, respectively). Systems encapsulated with 600 nm SiO_2 prepared by plasma-enhanced chemical vapor deposition (PECVD, 350 °C) show a lifetime of ≈5 min at 70 °C (Figure S3B, Supporting Information). The results here highlight the advantages of thermal oxide as biofluid barriers over other thin-film materials deposited by low-temperature processes. ALD Al_2O_3 and HfO_2 with high dielectric constant are also commonly used thin-film materials for encapsulation due to their strong coupling capability. Previous studies[33] show that coating a layer of ALD Al_2O_3 on top of Si nanowire transistors (with thermally grown SiO_2) can improve the stability of the device in the liquid environment due to the formation of tortuous diffusion pathways. However, results from a recent study[22] and this work suggest that using ALD metal oxide alone yields a shorter lifetime compared to t-SiO_2, as a lower growth temperature (<250 °C in this study) leads to a higher defect density in the film and a lower quality of the interface with the underlying layers.[34,35] In contrast, t-SiO_2 derived from monocrystalline Si has the advantage of a much higher film quality because of the high formation temperature (>1000 °C) and the structural integrity of the growth template. In this sense, SiO_2 can support the operation of active electronics in liquid environment with improved stability, which will be useful especially for systems where the lifetime of biochemical interface is relatively long (e.g., electrochemical fast-scan cyclic voltammetric method for DA detection).[36] For future applications, encapsulation materials should be properly chosen based on the stability of the sensing interfaces, the specific application scenarios (acute vs chronic), and the target lifetime of the sensing platform. The following strategies could be used to circumvent the weak coupling due to the lower dielectric constant of SiO_2: 1) opening a window on SiO_2 to establish a conductive pathway mediated by heavily doped Si, as illustrated in Figure 1; 2) decreasing the thickness of SiO_2 to reach a balance between the lifetime/stability and capacitance of the dielectric layer; and 3) enhancing the dimension of the laterally extended gate electrode buried under SiO_2 to avoid the voltage division effect. Results of bending tests (Figure 2F) show that key electrical performances of a t-SiO_2 encapsulated transistor remain nearly unchanged (bending radius: 8 mm, bending cycle: 100 and 200). Together, the stability of the

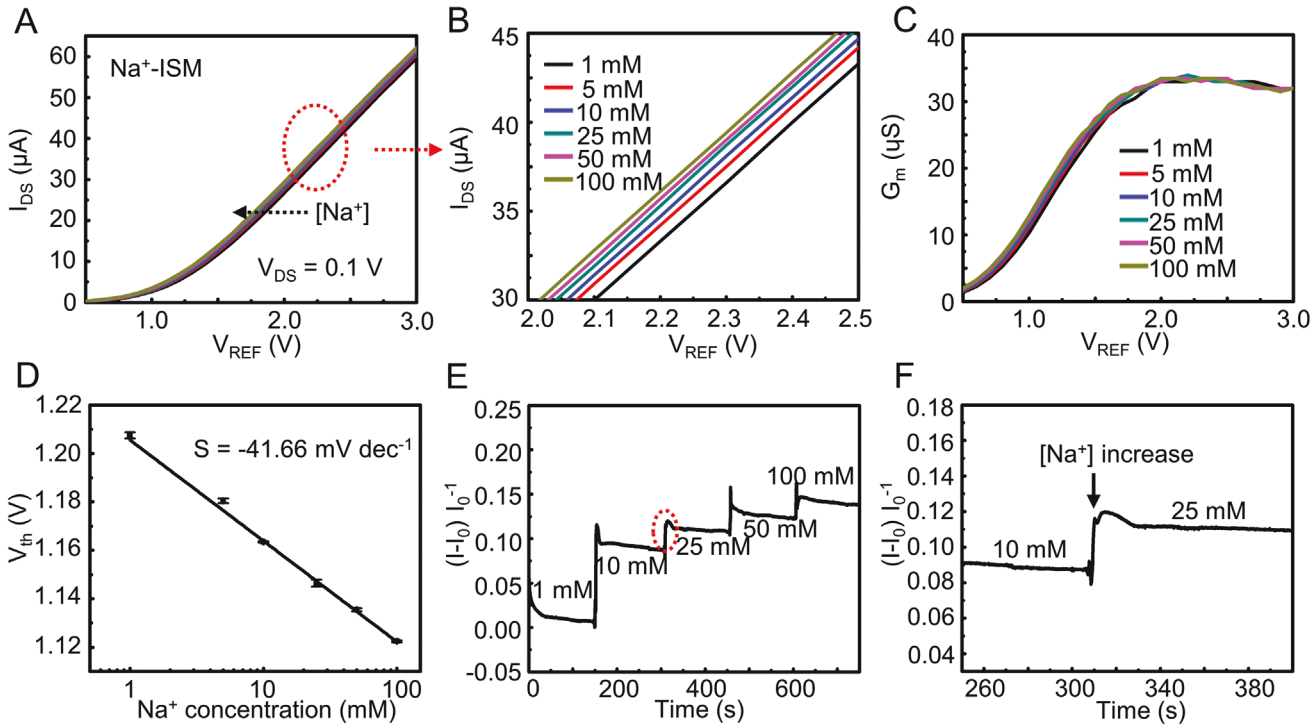

Figure 3. A) Transfer curves and B) zoom-in view of a representative Na^+ sensor in response to NaCl solutions with different concentrations. C) Transconductance (G_m) at different V_{REF} values derived from transfer curves. D) Sensitivity of the test device shown as the threshold voltage of the transistor as a function of Na^+ concentration (n = 3). E) Real-time response of drain-to-source current of the test device to changing Na^+ concentration. F) Zoom-in view of I_{DS} as a function of time showing the fast response of the ISM to changing Na^+ concentration. Data presentation: mean ± standard deviation.

ultrathin t-SiO_2 nanomembranes during leakage and bending tests serve as the foundation for developing waterproof and flexible biosensors.

2.3. Sensing Performance of Flexible FETs as Potentiometric Ion Sensors

Figure 3 shows the performance of a sensor with Na^+ ISM functionalized gate electrode in response to NaCl solutions with concentrations ranging from 1–100 mM. As shown in Figure 3A,B, an increasing Na^+ concentration causes a negative shift in the transfer curve, suggesting the addition of positive charges at the sensor-electrolyte interface. Extrapolating the tangent line of the transfer curve at the largest transconductance G_m value point (Figure 3C) extracts V_{th}. Plotting V_{th} values as a function of the concentration of Na^+ yields a sensitivity of –41.66 mV dec^{-1} (Figure 3D). The real-time response of the ISM to changing Na^+ concentration appears in Figure 3E,F. drain-to-source current (I_{DS}) changes upon the addition of concentrated Na^+ solutions with a response time of <5s. The absolute value of the sensitivity of the Na^+ sensor (41.66 mV dec^{-1}) in this work is within the range of the sensitivity of existing ion sensors (from 16 to 57 mV dec^{-1}) reported in literature (Table S2, Supporting Information). The fact that it is slightly lower than the highest reported value and the Nernst limit might be due to the non-ideal ratio of ionophores to ion exchangers and defects in the ISM, where further optimization is possible. The response time (≈ 5 s) is similar to those of other reported ion sensors (from 5 s to 1 min).

The study demonstrates the versatility of this device concept for potentiometric sensing by using the combination of waterproof transistors and other ISMs. Similarly, the results show high sensitivity, selectivity, and fast real-time response to corresponding target ions (K^+, Ca^{2+}, and H^+) as shown in **Figure 4**. In all cases, an increase in cation concentration results in a negative shift in V_{th} of the transfer curves (Figure 4A, D, G). Extracting the values of V_{th} as a function of ion concentration yields a sensitivity of –43.33 (K^+ ISM), –29.47 (Ca^{2+} ISM), and –56.93 (H^+ ISM) mV dec^{-1}, respectively (Figure 4B, E, H). The results are consistent with the Nernst limit calculated based on the valency of the corresponding ions. The I_{DS}-t curves of each type of sensor appear in Figure 4C, F,I. Key performance metrics of K^+, Ca^{2+}, and H^+ sensors are also comparable to reported values in literature (Table S3 to Table S5, Supporting Information). Tests in solutions with low concentrations of target ions evaluate the detection limit of the sensor systems. As shown in Figure S4A–C, Supporting Information, the lower detection limit of a H^+ FET sensor is around pH = 8.06. The value is close to that obtained using a H^+ ISM functionalized Au electrode (also around pH = 8.06, Figure S4D, Supporting Information). The results are consistent with previous reports that the detection limit of ISFETs often agrees with that of the ISM electrode of the same type.[37] Similarly, the lower detection limits of the Na^+ and K^+ sensors are estimated to be ≈1×10^{-5} and 1×10^{-6} M, respectively (Figure S4E,F, Supporting Information).

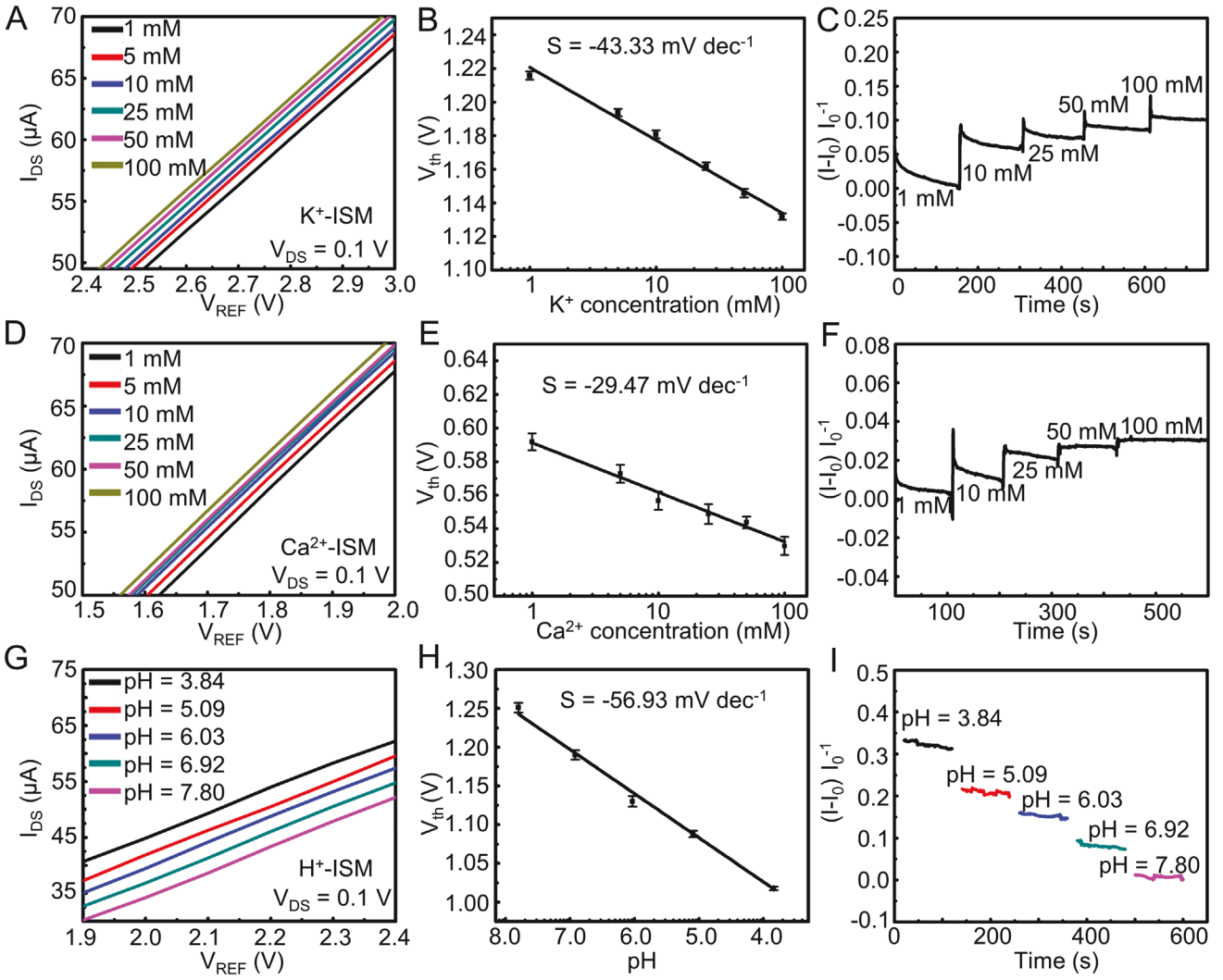

Figure 4. A) Zoom-in transfer curves of a K^+ sensor in response to KCl solutions with different concentrations. B) Sensitivity of the test device shown as the threshold voltage of the transistor as a function of K^+ concentration (n = 3). C) Real-time response of the test device to changing K^+ concentration. D) Zoom-in transfer curves of a Ca^{2+} sensor in response to $CaCl_2$ solutions with different concentrations. E) Sensitivity of the test device shown as the threshold voltage of the transistor as a function of Ca^{2+} concentration (n = 3). F) Real-time response of drain-to-source current of the test device to changing Ca^{2+}concentration. G) Zoom-in transfer curves of an H^+ sensor in response to solutions with different pH. H) Sensitivity of the test device shown as the threshold voltage of the transistor as a function of pH (n = 3). I) Drain-to-source current of the test device over time under different pH. Data presentation: mean ± standard deviation.

In general, this versatile, modularized sensor design exploiting the combination of the waterproof Si transistors and selective biochemical interfaces could enable the detection of different analyte species using the potentiometric sensing strategy by transducing changes in the surface potential upon the binding of analytes. Examples include peptides,[38] proteins,[39,40] nucleotide acids,[41] and others.[42–44]

2.4. Heavily Doped Si as Conductive Encapsulation for Amperometric Sensing

Besides potentiometric sensing outlined in the preceding section, one unique feature of the monolithic $Si-SiO_2$ biofluid barriers is the capability to support amperometric sensing. Here, a redox reaction occurring at the sensor-electrolyte interface can produce a charge transfer in the presence of an electrochemical potential via the heavily doped, highly conductive Si (resistivity: $\approx 10^{-3}$ Ω cm) to backplane electronics, while t-SiO_2 can serve as the passivation layer for the rest of the sensor system. Similar to t-SiO_2, p^{++}-Si has high structural integrity with a dissolution rate of ≈0.5 nm day^{-1} under physiological conditions.[45] **Figure 5**A shows the schematic illustration of an as-described working electrode encapsulated by the $Si-SiO_2$ nanomembranes. Depositing a layer of Au on top of the exposed p^{++}-Si forms an electrochemical interface for redox reactions and prevents the growth of SiO_X during dynamic electrochemistry.[46] The amperometric response can be characterized using a potentiostat with a three-electrode setup. Figure 5B presents an example of using such an encapsulated

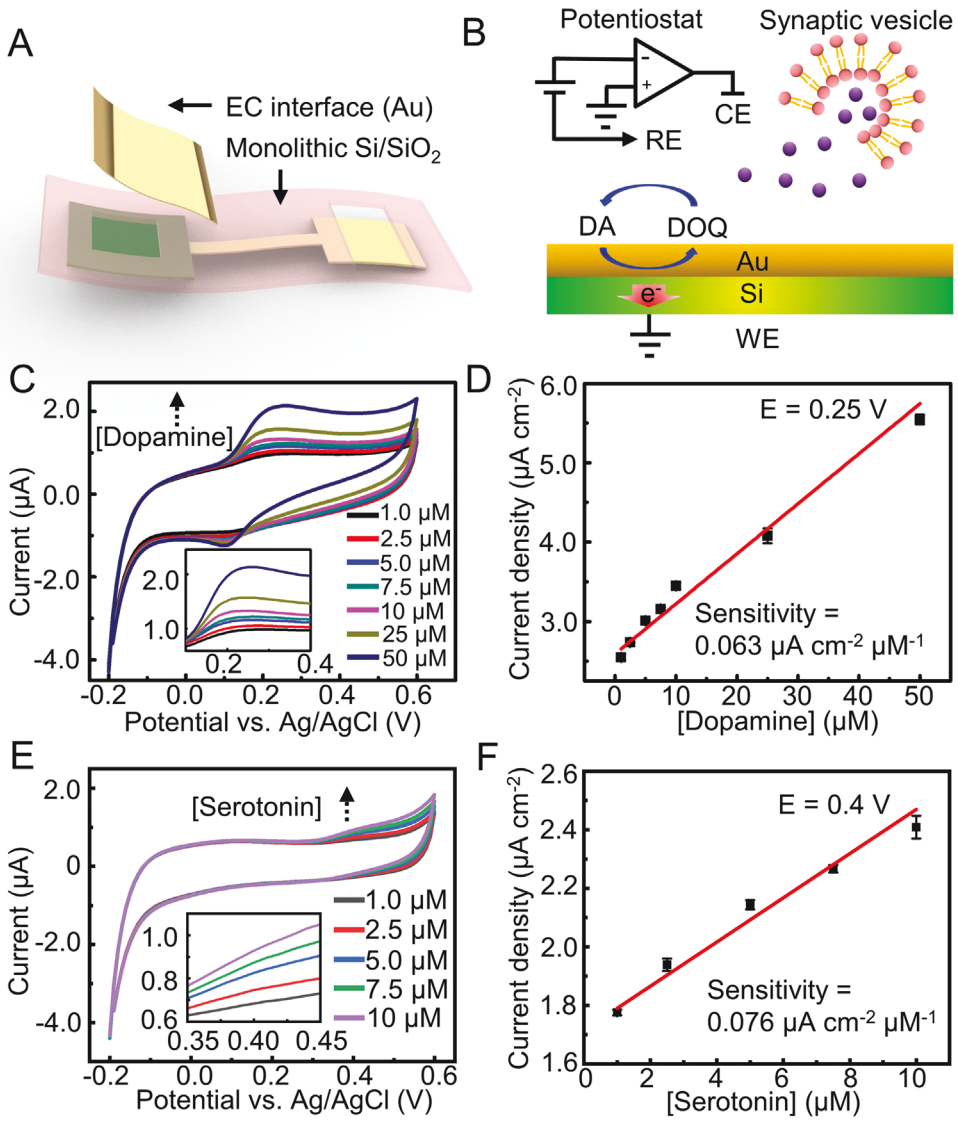

Figure 5. A) Schematic illustration of a flexible working electrode encapsulated with the monolithic Si—SiO_2 nanomembranes. B) Schematic illustration of using a Si—Au electrochemical interface for detecting DA through an amperometric sensing strategy. C) CV curves of an encapsulated system in solutions with varying DA concentrations. D) Current density at the oxidation peaks (E = 0.25 V) as a function of DA concentration (n = 3). E) CV curves of an encapsulated system in solutions with varying serotonin concentrations. F) Current density at the oxidation peaks (E = 0.4 V) as a function of serotonin concentration (n = 3). Data presentation: mean ± standard deviation.

system for detecting DA through the oxidation of DA to form dopamine o-quinone (DOQ). As presented in Figure 5C, cyclic voltammetry (CV) curves show stable oxidation and reduction peaks with varying DA concentrations (1–50 μM, scan rate (ν): 50 mV s^{-1}) (sensing surface area: 0.385 cm^2). Plotting the current density at the oxidation peaks (E = 0.25 V) as a function of DA concentration yields a sensitivity of 0.063 μA cm^{-2} μM^{-1} (Figure 5D). Another electroactive neurotransmitter, serotonin (1–10 μM, scan rate: 50 mV s^{-1}), shows an oxidation peak at 0.4 V during CV scan (Figure 5E), with a sensitivity of 0.076 μA cm^{-2} μM^{-1} (Figure 5F). On the other hand, CV scans in glucose and glutamate solutions only show negligible changes (Figure S5A,B, Supporting Information), suggesting a high selectivity of such waterproof electrodes to electroactive species at the corresponding redox peaks. Figure S5C–F, Supporting Information, show the CV scans of the Si—Au sensing interface obtained with different scan rates and plots of the oxidation peak current (i_{pa}) as a function of the square root of ν. The linear relationship suggests that both reactions are a diffusion-controlled process according to the Randles–Sevcik equation.[47] Such Si—SiO_2 nanomembranes encapsulated working electrodes can support the development of various flexible, waterproof electrochemical sensors. Integrating enzymes, electron mediators, and materials with high surface areas on the side of the encapsulation in contact with biofluids can improve the sensing performance (e.g., selectivity, sensitivity, limit of detection, and limit of quantification). Fabricating such p^{++}-Si-mediated working electrodes together with SiO_2 encapsulated active components following the integration scheme described in

Table 1. Ion concentrations and pH values of each solution used for establishing the sensitivity matrix *S*.

Concentration	Base solution (sol 1)	Na^+ solution 1 (sol 2)	Na^+ solution 2 (sol 3)	K^+ solution 1 (sol 4)	K^+ solution 2 (sol 5)	Ca^{2+} solution 1 (sol 6)	Ca^{2+} solution 2 (sol 7)	pH solution 1 (sol 8)	pH solution 2 (sol 9)
NaCl [mM]	40	70	100	40	40	40	40	40	40
KCl [mM]	5	5	5	10	25	5	5	5	5
$CaCl_2$ [mM]	0.37	0.37	0.37	0.37	0.37	1	5	0.37	0.37
pH	5.58	5.43	5.47	5.51	5.48	5.41	5.33	4.18	3.47

Figure 1 can further yield waterproof amperometric sensor arrays with on-chip multiplexing and signal amplification capabilities.

2.5. Multiplexed Arrays for Concurrent Ion Sensing

For in vivo application of such multiplexed sensor arrays, it is important that the system can concurrently and accurately sample changes in the concentration of multiple biomarkers. such as the ion fluxes in glial cells[48,49] and the disrupted ionic homeostasis resulting from secondary cell damages (e.g., stretching of axons) during TBI.[1] In a complex environment, the crosstalk sourced from non-specific interactions could be detrimental to the precise interpretation of sensing outcomes. To tackle this challenge, the study investigates responses of transistor arrays coupled with different ISMs to multiple ions in mixed solutions. The model assumes that in a mixed solution, the surface potential change in a potentiometric sensor can be viewed as the sum of surface potential changes caused by specific and non-specific interactions (Note S4, Supporting Information).

Measuring the responses of an array of ion sensors in a set of multi-ion solutions (**Table 1**) yields a sensitivity matrix *S* (unit: mV dec^{-1}) (**Figure 6**, Figures S6 and S7, Supporting Information):

$$S = \begin{bmatrix} S_{Na+Na+} & S_{Na+K+} & S_{Na+Ca2+} \\ S_{K+Na+} & S_{K+K+} & S_{K+Ca2+} \\ S_{Ca2+Na+} & S_{Ca2+K+} & S_{Ca2+Ca2+} \end{bmatrix} = \begin{bmatrix} -53.5 & 8.22 & 2.27 \\ 0 & -57.2 & -3.07 \\ 1.91 & 4.31 & -33.42 \end{bmatrix} \quad (1)$$

where S_{ii} and S_{ij} are the sensitivity of the sensor *i* to ion *i* (target analyte) and *j* (non-target analyte), respectively. The study also calculates response to changes in pH for potential applications with further enhanced multifunctionality. The following equation determines the concentration difference of *n* types of ions between an unknown solution and a standard reference solution, namely the vector Δc $(\Delta c_1, \Delta c_2, \ldots \Delta c_n)^T$,

$$\Delta c = S^{-1} \times \Delta V \quad (2)$$

where ΔV is a vector $(\Delta V_1, \Delta V_2, \ldots \Delta V_n)^T$ showing the response of the *n* ion-selective sensors in threshold voltage to the unknown solution.

Previous studies show that in CSF of TBI patients, the decrease in Na^+ concentration and increase in K^+ concentration are signs of the progression of secondary injury and condition worsening.[2,3] As shown in **Figure 7**A, in healthy brain tissues, Na^+ ions flow into neuron cells from the extracellular space through integral membrane proteins, producing a dendritic inward current. The accumulating positive charges caused by the influx of Na^+ are compensated by the function of the Na^+-K^+ pump which maintains the normal ion concentration gradient and the resting potential across the cell membrane by exporting Na^+ and importing K^+. During TBI, the decreased activity of the pump leads to an overall decrease in Na^+ concentration and an increase in K^+ concentration in CSF.[50] To validate the performance of the sensor arrays, the ion concentrations of an artificial solution mimicking the brain dialysis fluids of TBI patients (denoted as "aTBI" solution) are calibrated using the sensitivity matrix with an artificial CSF (aCSF) serving as a standard reference. Comparing V_{th} of the sensor arrays obtained in the aTBI solution with those obtained in the reference solution (Figure 7B–G) estimates the concentration of multiple ions (denoted as MATX method) (Note S5, Table S6, Supporting Information). Calculating the ion concentrations of the aTBI solution using the sensitivity obtained in single ion solutions provides comparison (denoted as SNGL method). The results and errors appear in **Table 2**. The concentrations of Na^+ and K^+ in the aTBI solution obtained using MATX method are very close to the actual values with small errors (Na^+:1.77%, K^+: 0.789%). On the other hand, errors for the measured ion concentration values using the SNGL method are much larger (Na^+: 16.8%, K^+: 8.68%), indicating the improved accuracy after calibration. The errors for the concentration of Ca^{2+} are relatively higher in both cases (>20%) consistent with previous reports,[1] which might be associated with the relatively smaller difference in Ca^{2+} concentration used here as well as the intrinsically lower Nernst limit for divalent ions. In all cases, the results suggest the importance of calibrating sensitivity in mixed ion solutions during multiplexed sensing for improved accuracy.

2.6. Stability of ISMs in Solution Under Physiological Condition

Long-term stability is a crucial yet challenging topic for implantable sensors. For biochemical sensing, the stabilities of the electronics and the sensing interfaces jointly determine the lifetime of the system. The unique "inverted fabrication" process and the resulting structure consisting of monocrystalline Si-derived nanomembranes as biofluid barriers can significantly improve the stability of electronics in liquid environment. However, the lifetime of ISMs under physiological conditions requires further investigation. The study characterizes the stability of ISM-functionalized Au surfaces in 1X PBS solution at 37 °C by measuring the open circuit potential (OCP) with an Ag/AgCl reference electrode. As illustrated in **Figure 8**A, a

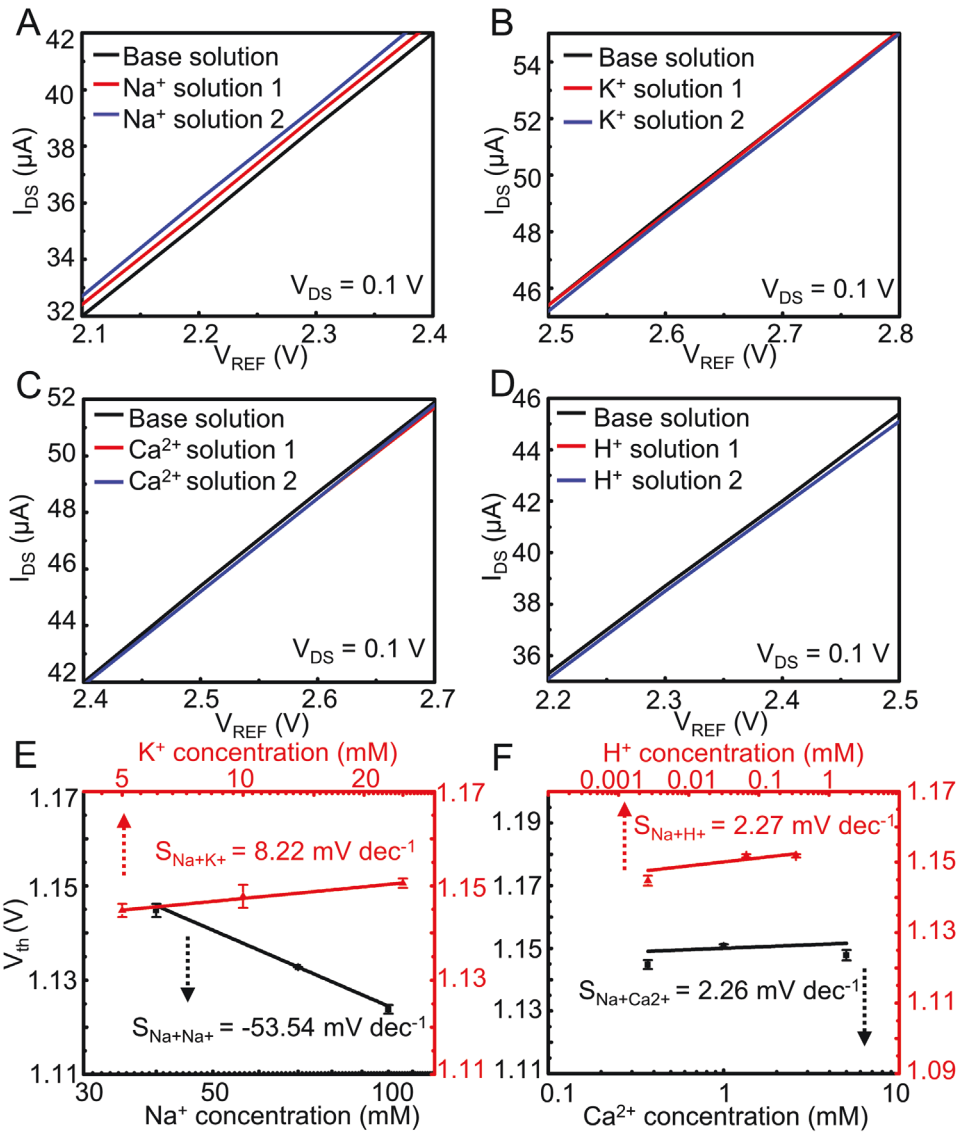

Figure 6. A–D) Zoom-in transfer curves of the Na^+ sensor in response to multi-ion solutions with varied Na^+, K^+, Ca^{2+}, and H^+ concentrations, respectively. E,F) Sensitivities of the Na^+ sensor shown as the threshold voltage of the transistor as a function of K^+, Na^+, Ca^{2+}, and H^+ concentrations (n = 3). Data presentation: mean ± standard deviation.

"co-extraction" process might take place during the immersion of ISMs in solutions.[9] An ISM typically consists of two key functional components: ionophores for capturing target ions, and lipophilic salts for providing ion exchange sites and reducing counter ionic interference. While anions typically do not enter cation-selective ISMs under a normal condition, a decreased number of ionic sites for cations can lead to a simultaneous migration of cations and anions into the membrane to maintain electrical neutrality, resulting in changes in sensitivity and selectivity.

The sensitivities of different ISMs towards their target ions over time (in 1X PBS at 37 °C) appear in Figure 8B. Both Na^+ and H^+ ISMs show good stability, maintaining a sensitivity of around ≈40 and ≈55 mV dec^{-1} for 4 weeks, respectively. When stored at an elevated temperature (59 °C), the Na^+ ISM still maintains a sensitivity of ≈40 mV dec^{-1} for at least a month (Figure S8A, Supporting Information). The sensitivity of the K^+ ISM slightly decreases from ≈45 to ≈35 mV dec^{-1} after 20 days, while the Ca^{2+} ISM only maintains a sensitivity above 20 mV dec^{-1} for a week which then drops to ≈5 mV dec^{-1} after 2 weeks. The lower stability of the Ca^{2+} ISM could be attributed to the plasticizer used in Ca^{2+} ISM (2-nitrophenyl octyl ether, (*o*-NPOE)): the higher polarity compared to that of the plasticizer (bis(2-ethylhexyl) sebacate, (DOS)) used in Na^+, K^+, and H^+ ISMs may increase its leaching rate from the ISM to the bulk solution.[51] The loss of plasticizer could change the membrane composition and the dielectric constant.[52] Previous studies show that the change in the dielectric constant of an ISM could have an impact on the ionophore-target stability.[53] Since the ionophore-target stability constant will affect the equilibrium concentration of the target ions in the ISM, the sensitivity will be altered accordingly.

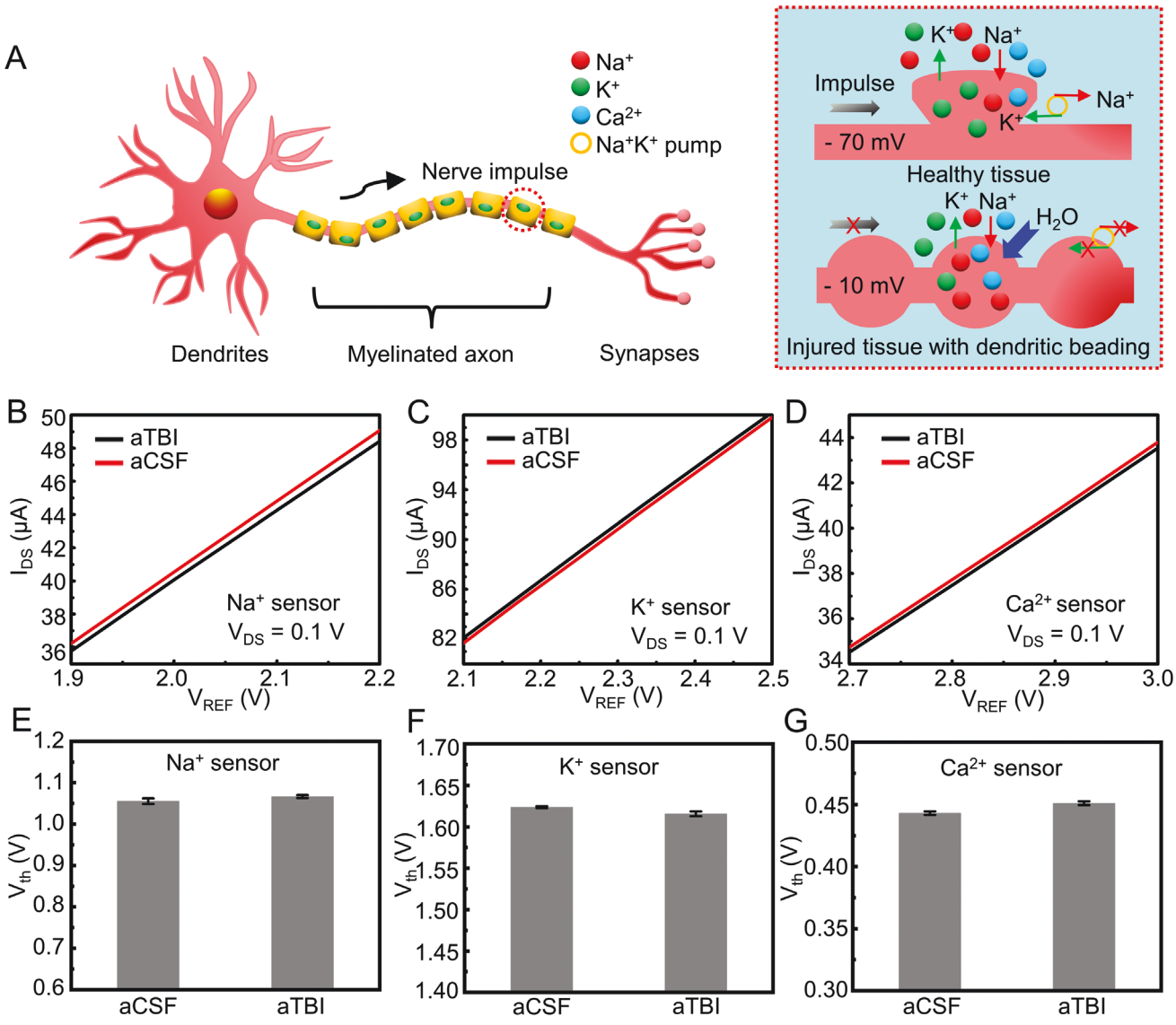

Figure 7. A) Schematic illustration of the ion fluxes under normal condition and during SD in TBI. B–D) Zoom-in transfer curves of the Na^+, K^+, and Ca^{2+} sensors in aCSF solution and aTBI solution. E–G) Summary of V_{th} of the Na^+, K^+, and Ca^{2+} sensors in aCSF solution and aTBI solution (n = 3). Data presentation: mean ± standard deviation.

Another important performance metric for long-term ion sensing is selectivity. Responses of each ISM to multiple ions appear in Figure 8C–F. After ≈4 weeks, the Na^+ ISM and H^+ ISM still maintain a high selectivity towards their corresponding target ions (Figure 8C,F and Figure S8B, Supporting Information), consistent with the observations in the sensitivity study. The Na^+ ISM shows a relatively high selectivity when stored at 59 °C (Figure S8C, Supporting Information). The K^+ ISM, however, develops a negative sensitivity in NaCl or $CaCl_2$ solutions over time (Figure 8D), suggesting a response to anions (Cl^-). One possible reason is that the lipophilic salt used in K^+ ISM, NaTPB, is more hydrophilic compared to NaTFPB and NaTClPB,[54] which may also promote the leaching process to the bulk solution. The loss of ionic sites caused by the leaching of NaTPB may cause the coextraction process,[9] leading to an additional response to the anions (Cl^-). This could also explain the slightly decreased sensitivity of the K^+ ISM after 3 weeks. The Ca^{2+} ISM shows a decreased selectivity towards Ca^{2+} mainly due to the significantly reduced response to Ca^{2+} (Figure 8E). Besides, the leaching of the plasticizer (*o*-NPOE) and thus the membrane composition could change

Table 2. Ion concentrations in aTBI solution measured and calculated using different methods. MATX represents the method using the sensitivity matrix, and SNGL represents the method using the sensitivities obtained in single ion solutions.

Ion species	aCSF [mM]	aTBI [mM]	Calculated aTBI MATX [mM]	Error %	Calculated aTBI SNGL [mM]	Error %
Na^+ [mM]	147	96.2	94.5	1.77	80.0	16.8
K^+ [mM]	2.7	3.8	3.83	0.789	4.13	8.68
Ca^{2+} [mM]	1.2	0.99	0.705	28.8	0.642	35.2

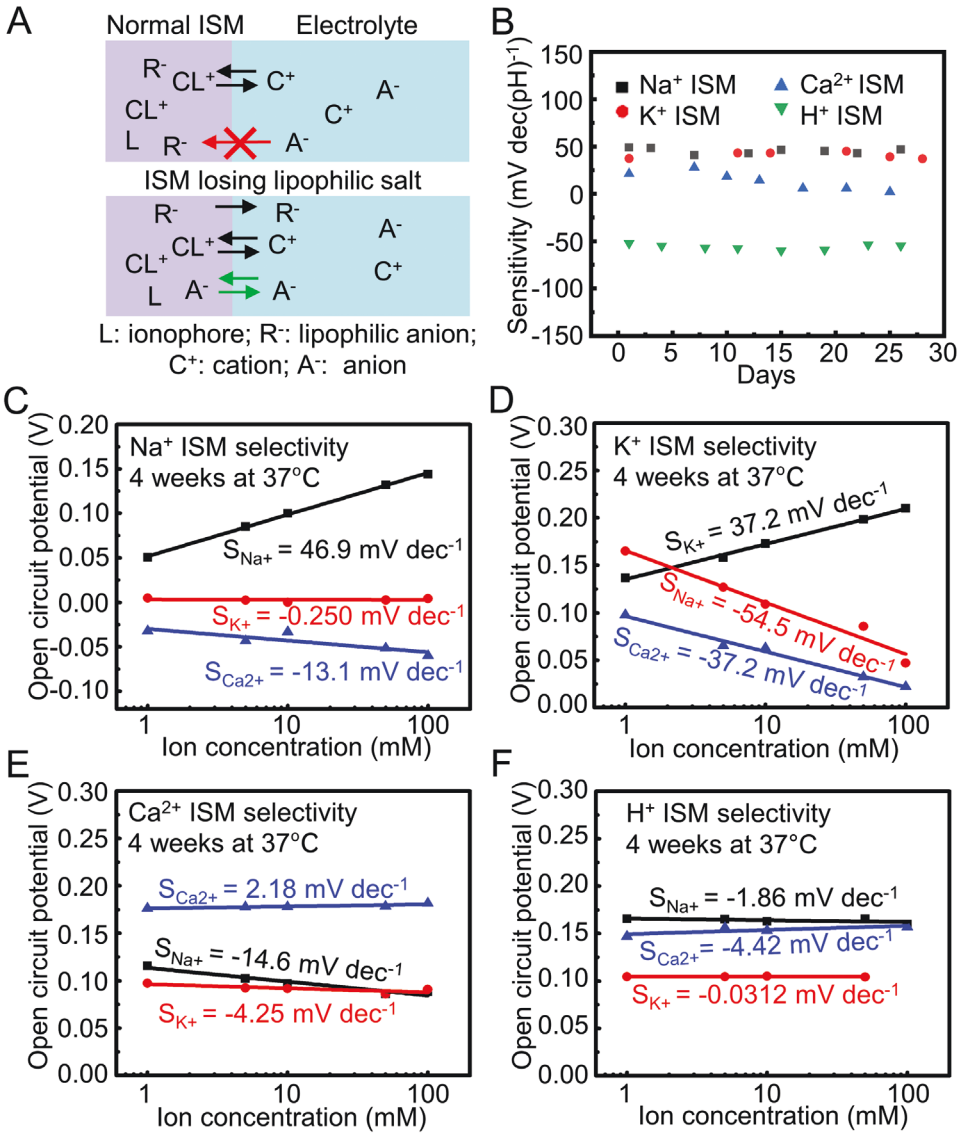

Figure 8. A) Schematic illustration of the coextraction process due to the leaching of lipophilic anions from ISM to bulk solution. Under normal condition, anions in the solution cannot enter the ISM (top), while in an ISM losing lipophilic anion R^- (bottom), cations (C^+), and anions (A^-) are coextracted into the membrane to maintain the electrical neutrality. B) Sensitivity of Na^+, K^+, Ca^{2+}, and H^+ ISMs to target ions during immersion tests in 1X PBS solution at 37 °C. C–F) Response of Na^+, K^+, Ca^{2+}, and H^+ ISMs to multiple ions during immersion tests in 1X PBS solution at 37 °C for 4 weeks.

the dielectric constant of the ISM, which may also affect the selectivity of the ISM.[52,55] The results suggest that multiple factors such as the choices of plasticizers and ion exchangers may play important roles in determining the performance of ISMs in solution during long-term application. Further improvements are possible through systematic studies on the structure-property interrelationship and rational designs to obtain extended lifetimes.

2.7. Ion Sensing in Real Human Sample

To demonstrate the sensing performance in a complex environment with human-related samples, this study performs pH sensing tests in human serum (Sigma Aldrich, H4522, lot# SLCJ3948, from human male AB plasma, USA origin, sterile filtered). Coating the Au surface of the gate electrode with polyaniline (PANI) through electrodeposition forms a pH-sensitive interface (0.25 M aniline in 0.5 M H_2SO_4, −0.2–1 V vs Ag/AgCl, 10 cycles). Detailed test results in pH buffer solutions and the human serum sample appear in Figure S9, Supporting Information. The system shows a sensitivity of 57.9 mV pH^{-1}. Calculating the pH value of the serum sample based on the calibration curve yields a value of ≈7.8, which is close to the one obtained using a commercial pH meter (7.63). The results suggest that such sensors have a practical sensing capability that can be potentially expanded for detection of other biomarkers.

3. Conclusion

In summary, the results presented here provide materials strategies, interface designs, and integration schemes for building flexible, waterproof, and multiplexed MOSFET biochemical sensor arrays. The design of the ultrathin biofluid barriers exploiting the monolithic p^{++}-Si and t-SiO_2 nanomembranes is compatible with potentiometric and amperometric sensing strategies, thereby offering unique advantages in developing waterproof, active electronics for high-fidelity, continuous monitoring of different types of neurological biomarkers (e.g., ions and neurotransmitters) in liquid environment. To improve the precision for concurrent multi-ion sensing, calibration standards address the cross-sensitivity issue caused by non-specific interactions between ISMs and non-target ions. The sensor arrays can capture minute changes in concentrations of multiple ions in artificial solutions mimicking CSFs from TBI patients, suggesting their great potential as in vivo recording devices for the early diagnosis of secondary TBI. Systematic studies investigate failure mechanisms of ISMs during immersion tests associated with the leaching of functional components under physiological conditions. The study opens a pathway to scalable fabrication of waterproof biochemical sensor arrays using SOI substrates and standard complementary metal-oxide-semiconductor (CMOS) technologies. Integration of different bio-recognition elements can expand the device concept for efficient detection of various biomarkers using potentiometry and/or amperometry. Stable but ultimately bioresorbable active systems are also possible by replacing metals and polymers used here with transient counterparts (e.g., Zn, Mg).[56–58] The results may create new opportunities for understanding the body's dynamic chemistry over extended periods during biomedical research and clinical practices. Future directions include the development of waterproof, high-resolution, and fully integrated chemical sensor arrays with local active components for mapping the spatiotemporal distribution of neuronal compounds, as well as multifunctional neural interfaces with integrated, miniaturized biochemical sensors and neural electrodes for dual-mode recording.

4. Experimental Section

Fabrication of Encapsulated, Waterproof Si MOSFET: The development of MOSFETs with ultrathin, waterproof interfaces included four essential steps: transistor fabrication, polymer coating, back etching, and via opening (more details in Figure S2, Supporting Information). Briefly, the process started with two cycles of deposition, patterning, and doping of device grade Si on a SOI wafer (Soitec) following standard semiconductor processing techniques to form isolated n^{++} regions as the source and drain of the transistor and p^{++} regions as the electrically conductive interface. The reason for choosing p^{++}-Si as the conductive encapsulation was due to its higher stability than n^{++}-Si in biofluids.[45] Thermal oxidation followed by ALD formed a layer of SiO_2 (≈50 nm) and a layer of Al_2O_3 (≈10 nm) as the gate dielectric stack. Photolithographically patterning, etching, and metallization (10 nm Cr/300 nm Au) completed the fabrication of FETs. Spin-coating of polyimide (PI) precursor followed by thermal curing formed a thin PI film (≈2 µm) on top of the transistors. A commercial silicone adhesive layer then joined the PI layer and a temporary handling substrate with a spin-coated polydimethylsiloxane (PDMS) and a laminated Kapton film (≈13 µm). Inductively coupled plasma RIE (ICP-RIE) with SF_6/O_2 removed the Si handle wafer to expose the buried t-SiO_2 as the submicron encapsulation layer. Photolithographic patterning and combined dry (CF_4)/wet (buffered oxide etch (BOE), 10:1) etching formed via opening on SiO_2 aligned to the underlying p^{++}-Si. A probe station and a semiconductor parameter analyzer (Keysight B1500A) characterized the electrical performance of the transistors.

Leakage Tests for Thin Film Materials: The study used PBS solution to provide an environment for the leakage test of thin films including t-SiO_2 and ALD-Al_2O_3/HfO_2. An oven controlled the temperature of the systems. An electrochemical station measured the leakage current across the thin films as a function of time to determine the leakage (defined as >1 nA cm^{-2}).

Preparation and Characterization of p^{++}-Si Mediated Amperometric Sensors: Electron-beam evaporation formed a bilayer of Cr/Au (5/50–200 nm) on the p^{++}-Si surface as the working electrode for electrochemical sensing (it should be noted that for a fully integrated system, thermal evaporation should be used to avoid electron radiation induced shift in the threshold voltage of the transistors). CV using an electrochemical station (PALM-PS4.F2.10) characterized the response to DA, serotonin, glucose, and glutamate solutions with a platinum wire as the counter electrode and a saturated Ag/AgCl electrode as the reference electrode.

Preparation of ISMs: The sodium-selective membrane consisted of sodium ionophore X (1 wt.%), sodium tetrakis[3,5-bis(trifluoromethyl)-phenyl] borate (Na-TFPB, 0.55 wt.%, providing cation exchange sites and reducing resistance), polyvinyl chloride (PVC, 33 wt.%, plastic matrix), and bis(2-ethylhexyl) sebacate (DOS, 65.45 wt.%, plasticizer). Dissolving 100 mg of the mixture mentioned above in 660 µL tetrahydrofuran yielded the sodium ISM cocktail. The potassium-selective membrane consisted of valinomycin (2% wt.%, ionophore), sodium tetraphenylborate (Na-TPB 0.5 wt.%, providing cation exchange sites and reduce resistance), PVC (32.7 wt.%, plastic matrix), and DOS (64.7 wt.%, plasticizer). Dissolving 100 mg of the mixture mentioned above in 350 µL of cyclohexanone formed the potassium ISM cocktail. The calcium-selective membrane cocktail was purchased from Sigma Aldrich and used directly. The composition of the calcium-selective membrane cocktail was calcium ionophore IV (0.072 wt.%, ionophore), Na-TFPB (0.022 wt.%, providing cation exchange sites and reduce resistance), 2-nitrophenyl octyl ether (4.748 wt.%, plasticizer), PVC (2.379 wt.%, plastic matrix), and tetrahydrofuran (92.78 wt.%, solvent). The hydrogen-selective membrane consisted of hydrogen ionophore I (1 wt.%, ionophore), Na-TClPB (0.65 wt.%, providing cation exchange sites and reduce resistance), PVC (33 wt.%, plastic matrix), and DOS (65.35 wt.%, plasticizer). Dissolving 100 mg of the mixture mentioned above in 660 µL tetrahydrofuran formed the hydrogen ISM cocktail. Drop-casting of as-prepared mixtures on Au surfaces followed by drying at room temperature overnight formed various ISM sensing interfaces as gate electrodes of the transistors for potentiometric sensing.

Statistical Analysis: Raw data were used directly for analysis without preprocessing. Data were expressed as mean ± standard deviation (SD). The sample size (n) for each statistical analysis was 3. Linear regression (V_{th}/OCP vs logarithm of ion concentration) determined the sensitivity of the system. OriginPro was used for data analysis.

Supporting Information

Supporting Information is available from the Wiley Online Library or from the author.

Acknowledgements

This work was supported by The Ohio State University start-up funds, the Chronic Brain Injury Pilot Award Program, and the National Center For Advancing Translational Sciences (Award Number: UL1TR002733).

The content is solely the responsibility of the authors and does not necessarily represent the official views of the National Center For Advancing Translational Sciences or the National Institutes of Health. This work was also supported in part by The Ohio State University Materials Research Seed Grant Program, funded by the Center for Emergent Materials, an NSF-MRSEC, grant DMR-2011876, the Center for Exploration of Novel Complex Materials, and the Institute for Materials Research.

Conflict of Interest

The authors declare no conflict of interest.

Author Contributions

J.L. and Y.D. conceived the design of the project; Y.D. performed the experiments and data analysis. S.C and T.L. performed the experiments and data collection for electrochemical sensing. All authors contributed to writing the manuscript and have approved the final version of the manuscript.

Data Availability Statement

The data that support the findings of this study are available from the corresponding author upon reasonable request.

Keywords

amperometry, field-effect transistors, flexible electronics, multiplexed sensing, potentiometry

Received: November 8, 2021
Revised: December 5, 2021
Published online: January 13, 2022

[1] N. Moser, C. L. Leong, Y. Hu, C. Cicatiello, S. Gowers, M. Boutelle, P. Georgiou, *Anal. Chem.* **2020**, *92*, 5276.
[2] J. J. Hablitz, U. Heinemann, *Dev. Brain Res.* **1989**, *46*, 243.
[3] M. L. Rogers, C. L. Leong, S. A. N. Gowers, I. C. Samper, S. L. Jewell, A. Khan, L. McCarthy, C. Pahl, C. M. Tolias, D. C. Walsh, A. J. Strong, M. G. Boutelle, *J. Cereb. Blood Flow Metab.* **2016**, *37*, 1883.
[4] R. Bullock, A. Zauner, J. J. Woodward, J. Myseros, S. C. Choi, J. D. Ward, A. Marmarou, H. F. Young, *J. Neurosurg.* **1998**, *89*, 507.
[5] S. S. Koura, E. M. R. Doppenberg, A. Marmarou, S. Choi, H. F. Young, R. Bullock, *Acta Neurochir., Suppl.* **1998**, *71*, 244.
[6] R. Chamoun, D. Suki, S. P. Gopinath, J. C. Goodman, C. Robertson, *J. Neurosurg.* **2010**, *113*, 564.
[7] J. Viventi, D.-H. Kim, L. Vigeland, E. S. Frechette, J. A. Blanco, Y.-S. Kim, A. E. Avrin, V. R. Tiruvadi, S.-W. Hwang, A. C. Vanleer, D. F. Wulsin, K. Davis, C. E. Gelber, L. Palmer, J. Van der Spiegel, J. Wu, J. Xiao, Y. Huang, D. Contreras, J. A. Rogers, B. Litt, *Nat. Neurosci.* **2011**, *14*, 1599.
[8] H. Fang, K. J. Yu, C. Gloschat, Z. Yang, E. Song, C.-H. Chiang, J. Zhao, S. M. Won, S. Xu, M. Trumpis, Y. Zhong, S. W. Han, Y. Xue, D. Xu, S. W. Choi, G. Cauwenberghs, M. Kay, Y. Huang, J. Viventi, I. R. Efimov, J. A. Rogers, *Nat. Biomed. Eng.* **2017**, *1*, 0038.
[9] E. Bakker, P. Bühlmann, E. Pretsch, *Chem. Rev.* **1997**, *97*, 3083.
[10] S. Nakata, M. Shiomi, Y. Fujita, T. Arie, S. Akita, K. Takei, *Nat. Electron.* **2018**, *1*, 596.
[11] P. Bergveld, *Sens. Actuators, B* **2003**, *88*, 1.
[12] M. Kaisti, *Biosens. Bioelectron.* **2017**, *98*, 437.
[13] S. Libertino, S. Conoci, A. Scandurra, C. Spinella, *Sens. Actuators, B* **2013**, *179*, 240.
[14] B. Liu, L. Chen, G. Liu, A. N. Abbas, M. Fathi, C. Zhou, *ACS Nano* **2014**, *8*, 5304.
[15] A. N. Abbas, B. Liu, L. Chen, Y. Ma, S. Cong, N. Aroonyadet, M. Köpf, T. Nilges, C. Zhou, *ACS Nano* **2015**, *9*, 5618.
[16] Y. Liang, M. Xiao, D. Wu, Y. Lin, L. Liu, J. He, G. Zhang, L.-M. Peng, Z. Zhang, *ACS Nano* **2020**, *14*, 8866.
[17] Q. Liu, C. Zhao, M. Chen, Y. Liu, Z. Zhao, F. Wu, Z. Li, P. S. Weiss, A. M. Andrews, C. Zhou, *Iscience* **2020**, *23*, 101469.
[18] C. Zhao, Q. Liu, K. M. Cheung, W. Liu, Q. Yang, X. Xu, T. Man, P. S. Weiss, C. Zhou, A. M. Andrews, *ACS Nano* **2020**, *15*, 904.
[19] Q. Liu, Y. Liu, F. Wu, X. Cao, Z. Li, M. Alharbi, A. N. Abbas, M. R. Amer, C. Zhou, *ACS Nano* **2018**, *12*, 1170.
[20] A. Topkar, R. Lal, *Thin Solid Films* **1993**, *232*, 265.
[21] H. Li, Y. Zhu, M. S. Islam, M. A. Rahman, K. B. Walsh, G. Koley, *Sens. Actuators, B* **2017**, *253*, 759.
[22] H. Fang, J. N. Zhao, K. J. Yu, E. M. Song, A. B. Farimani, C. H. Chiang, X. Jin, Y. G. Xue, D. Xu, W. B. Du, K. J. Seo, Y. D. Zhong, Z. J. Yang, S. M. Won, G. H. Fang, S. W. Choi, S. Chaudhuri, Y. G. Huang, M. A. Alam, J. Viventi, N. R. Aluru, J. A. Rogers, *Proc. Natl. Acad. Sci. USA* **2016**, *113*, 11682.
[23] V. T. Ivanov, I. A. Laine, N. D. Abdulaev, L. B. Senyavina, E. M. Popov, Y. A. Ovchinnikov, M. M. Shemyakin, *Biochem. Biophys. Res. Commun.* **1969**, *34*, 803.
[24] M. M. Shemyakin, Y. A. Ovchinnikov, V. T. Ivanov, V. K. Antonov, E. I. Vinogradova, A. M. Shkrob, G. G. Malenkov, A. V. Evstratov, I. A. Laine, E. I. Melnik, I. D. Ryabova, *J. Membr. Biol.* **1969**, *1*, 402.
[25] V. V. Egorov, Y. F. Lushchik, *Talanta* **1990**, *37*, 461.
[26] I. Fakih, O. Durnan, F. Mahvash, I. Napal, A. Centeno, A. Zurutuza, V. Yargeau, T. Szkopek, *Nat. Commun.* **2020**, *11*, 3226.
[27] D. Lee, W. H. Jung, S. Lee, E.-S. Yu, T. Lee, J. H. Kim, H. S. Song, K. H. Lee, S. Lee, S.-K. Han, M. C. Choi, D. J. Ahn, Y.-S. Ryu, C. Kim, *Nat. Commun.* **2021**, *12*, 3741.
[28] S. Sheibani, L. Capua, S. Kamaei, S. S. A. Akbari, J. Zhang, H. Guerin, A. M. Ionescu, *Commun. Mater.* **2021**, *2*, 10.
[29] H.-P. Phan, Y. Zhong, T.-K. Nguyen, Y. Park, T. Dinh, E. Song, R. K. Vadivelu, M. K. Masud, J. Li, M. J. Shiddiky, D. Dao, Y. Yamauchi, J. A. Rogers, N.-T. Nguyen, *ACS Nano* **2019**, *13*, 11572.
[30] T. A. Pham, T. K. Nguyen, R. K. Vadivelu, T. Dinh, A. Qamar, S. Yadav, Y. Yamauchi, J. A. Rogers, N. T. Nguyen, H. P. Phan, *Adv. Funct. Mater.* **2020**, *30*, 2004655.
[31] S. Chen, Y. Dong, T.-L. Liu, J. Li, *Biosens. Bioelectron.* **2022**, *195*, 113683.
[32] K. Brown, *Proc. Int. Workshop Miner. Scaling* **2011**, 25.
[33] O. Knopfmacher, A. Tarasov, W. Fu, M. Wipf, B. Niesen, M. Calame, C. Schönenberger, *Nano Lett.* **2010**, *10*, 2268.
[34] M. L. Chang, L. C. Wang, H. C. Lin, M. J. Chen, K. M. Lin, *Appl. Surf. Sci.* **2015**, *359*, 533.
[35] S. Li, Y. Zhang, D. Yang, W. Yang, X. Chen, H. Zhao, J. Hou, P. Yang, *Phys. B* **2020**, *584*, 412065.
[36] H. N. Schwerdt, H. Shimazu, K.-i. Amemori, S. Amemori, P. L. Tierney, D. J. Gibson, S. Hong, T. Yoshida, R. Langer, M. J. Cima, A. M. Graybiel, *Proc. Natl. Acad. Sci. USA* **2017**, *114*, 13260.
[37] A. Bratov, N. Abramova, C. Domínguez, *Talanta* **2004**, *62*, 91.
[38] I. Sarangadharan, S.-L. Wang, T.-Y. Tai, A. K. Pulikkathodi, C.-P. Hsu, H.-H. K. Chiang, L. Y.-M. Liu, Y.-L. Wang, *Biosens. Bioelectron.* **2018**, *107*, 259.
[39] S. P. White, S. Sreevatsan, C. D. Frisbie, K. D. Dorfman, *ACS Sens.* **2016**, *1*, 1213.

[40] P. Estrela, D. Paul, Q. Song, L. K. J. Stadler, L. Wang, E. Huq, J. J. Davis, P. K. Ferrigno, P. Migliorato, *Anal. Chem.* **2010**, *82*, 3531.
[41] W.-C. Kuo, I. Sarangadharan, A. K. Pulikkathodi, P.-H. Chen, S.-L. Wang, C.-R. Wu, Y.-L. Wang, *Sensors* **2019**, *19*, 1484.
[42] J. Kim, Y. S. Rim, H. Chen, H. H. Cao, N. Nakatsuka, H. L. Hinton, C. Zhao, A. M. Andrews, Y. Yang, P. S. Weiss, *ACS Nano* **2015**, *9*, 4572.
[43] B.-R. Li, Y.-J. Hsieh, Y.-X. Chen, Y.-T. Chung, C.-Y. Pan, Y.-T. Chen, *J. Am. Chem. Soc.* **2013**, *135*, 16034.
[44] N. Nakatsuka, K.-A. Yang, J. M. Abendroth, K. M. Cheung, X. Xu, H. Yang, C. Zhao, B. Zhu, Y. S. Rim, Y. Yang, P. S. Weiss, M. N. Stojanović, A. M. Andrews, *Science* **2018**, *362*, 319.
[45] J. H. Li, E. M. Song, C. H. Chiang, K. J. Yu, J. Koo, H. N. Du, Y. S. Zhong, M. Hill, C. Wang, J. Z. Zhang, Y. S. Chen, L. M. Tian, Y. D. Zhong, G. H. Fang, J. Viventi, J. A. Rogers, *Proc. Natl. Acad. Sci. USA* **2018**, *115*, E9542.
[46] V. R. Gonçales, J. Lian, S. Gautam, R. D. Tilley, J. J. Gooding, *Annu. Rev. Anal. Chem.* **2020**, *13*, 135.
[47] N. Elgrishi, K. J. Rountree, B. D. McCarthy, E. S. Rountree, T. T. Eisenhart, J. L. Dempsey, *J. Chem. Educ.* **2018**, *95*, 197.
[48] Y. Zhu, G. Koley, K. Walsh, A. Galloway, P. Ortinski, *IEEE Sens.* **2016**, 1.
[49] K. B. Walsh, N. DeRoller, Y. Zhu, G. Koley, *Biosens. Bioelectron.* **2014**, *54*, 448.
[50] J. P. Dreier, *Nat. Med.* **2011**, *17*, 439.
[51] A. Kisiel, D. Kałuża, B. Paterczyk, K. Maksymiuk, A. Michalska, *Analyst* **2020**, *145*, 2966.
[52] R. Eugster, T. Rosatzin, B. Rusterholz, B. Aebersold, U. Pedrazza, D. Rüegg, A. Schmid, U. E. Spichiger, W. Simon, *Anal. Chim. Acta* **1994**, *289*, 1.
[53] M. C. Rose, R. W. Henkens, *Biochim. Biophys. Acta, Gen. Subj.* **1974**, *372*, 426.
[54] M. Telting-Diaz, E. Bakker, *Anal. Chem.* **2001**, *73*, 5582.
[55] U. Oesch, W. Simon, *Anal. Chem.* **1980**, *52*, 692.
[56] I. Cockerill, Y. Su, J. H. Lee, D. Berman, M. L. Young, Y. Zheng, D. Zhu, *Nano Lett.* **2020**, *20*, 4594.
[57] D. Zhu, J. You, N. Zhao, H. Xu, *Adv. Sci.* **2019**, *6*, 1901166.
[58] S.-K. Kang, J. Koo, Y. K. Lee, J. A. Rogers, *Acc. Chem. Res.* **2018**, *51*, 988.